Synthesis of Nanostructures of Iron Binary/Ternary Phased Sulfide/Selenide by Hot Injection Method and Case Study for The Removal of Carcinogenic Dye Red S3B *Via* Photocatalysis

Rehana Akram
Javeed Akhtar (javeedkt@gmail.com)
Mirpur University of Science and Technology https://orcid.org/0000-0001-5938-3315
Humaira Rashid Khan
Masood Akhtar
Mohammad Azad Malik
Neerish Revaprasadu
Yousef AlGhamdi
Moazzam H. Bhatti

Research Article

Keywords:

Posted Date: February 22nd, 2022

DOI: https://doi.org/10.21203/rs.3.rs-1366654/v1

Abstract

Iron based nanoplates of iron sulfide (FeS_2), iron selenide ($FeSe_2$) and iron sulfo selenide (FeS_xSe_{1-x}) have been synthesised in one pot by using Fe(III) or Fe(II) chloride as iron source and sulfur or selenium powder as S and Se source in oleylamine. These synthesised nanoplates were characterized by x-rays diffraction (XRD), Transmission electron microscopy (TEM), High resolution transmission electron microscopy and energy dispersion x-rays (EDX) spectroscopy. These materials were also investigated for their performance as photocatalysts for the degradation of a carcinogenic industrial dye RS3B under solar light. The comparison of crystallinity, dimensions, yields and electronic properties of these synthesised nanoplates with respect to the use of Fe (II) or Fe (III) as iron source and also the synthesis carried out at 30 minutes and one hour show that Fe (II) is better source for iron and the synthesis carried out at 30 minutes give much better quality materials that those synthesized for one hour. This observation was true for all three materials (FeS_2, $FeSe_2$ and FeSSe).

1. Introduction

Transition metal based nanoparticles has been given much attention because of its unusual structure and electronic properties. Among III–VI group compounds, iron sulphide/selenide have great importance, because of their potential use as an absorber in solar cells [1, 2]. The materials such as Cd, Pb, In, *etc.* currently used for photovoltaic application are either toxic or non-abundant and cannot contribute significantly to a future sustainable energy supply.[3, 4] For this reason non-toxic, abundant, and cheap materials with less efficiencies are acceptable for photovoltaic applications. The iron and copper sulfide are most promising materials for photovoltaic applications [3, 5–11].

Unlike iron oxide nanoparticles and thin films, which have long been studied, the chalcogenide counterparts have historically received less attention, though this has changed in recent years [12]. The most studied applications for iron chalcogenides are as photovoltaics or supercapacitors, with considerable research [13–16]. Most of the applications require a very precisely defined morphology in order to maximise current flow whilst minimising hole-electron recombination at defect sites [17]. Only pyrite (FeS_2) demonstrates photoactivity, and contamination with secondary phases is prone to reduce the efficiency of devices [18].

Iron sulphide nanocrystals [19, 20] have been prepared with hydrothermal methods [21–23]. One-dimensional (1-D) nanostrurtures of FeS_2 (cubic pyrite) were synthesized by solvothermal process at low temperature [24, 25]. Cubic Pyrite (FeS_2) nanorods, nanowires and ribbon like nanostructures were obtained by altering the molar concentration of the reactants or by changing growth temperature [26][27]. Morphology and size controlled synthesis of pyrite with direct and indirect band gap ranging from 0.89 to 1.2 eV have been reported [28–32]. Cummins *et al* [33] synthesized the phase pure iron sulphide (FeS) nanowires by sulfurization of hematite nanowire arrays. Hexagonal plate and prism and nanoflowers morphologies of the pyrrhotite ($Fe_{1-x}S$ (Fe_7S_8)) and greigite (Fe_3S_4) phase with average size of 70 nm has been reported [34–36]. *Bis*(tetra-n-butylammonium)-tetrakis[benzenethiolato-μ_3-sulfido iron][37]

tris(diethydithiophosphato)iron(III) [38] poly sulfide iron(*N*-methylimidazole (*N*-MeIm)) [39] iron(III) complex of 1,1,5,5-tetra-*iso*-propyl-2-thiobiuret [40] *tris*(*O*-alkylxanthato)iron(III) complexes [41] have been used as single source precursors by thermolysis in different capping agents for the synthesis of iron sulfide nanoplates. Mixed and pure phases of iron sulfide nanocrystals were produced from these single source precursors at different growth temperatures [21, 42, 43].

Bi *et al* [44] deposited the thin films of pure pyrite (FeS_2) phase by dip coating. The films showed optical band gaps of 0.93 eV (indirect) and 1.38 eV (direct) with high absorption efficiency ($\sim 2 \times 10^5$ cm^{-1}). Symmetrical and unsymmetrical dithiocarbamate iron (III) complexes are used [45] as single source precursors for the deposition of iron sulfide thin films by Aerosol Assisted Chemical Vapour Deposition (AACVD) method. Li *et al* [46] reported that the conductivity and photoconductivity of pyrite nanocrystals can be tuned over four orders of magnitude by employing different anchor groups and both aliphatic and aromatic bridging groups.

Like iron sulfide iron selenide is also an attractive material having a direct band gap of 1.23 eV, which makes it quite efficient for solar cells. Iron selenide (FeSe) could be semiconductors or even superconductors with characteristics of ferro/ferrimagnetic materials [47, 48]. The conductive properties of iron selenide (FeSe) depends on the composition of the material.

A number of methods have been applied for the synthesis of iron selenide nanocrystals. Hexagonal (H) and monoclinic (M) iron selenide nanocrystals with NiAs-like structure were synthesized in one-pot thermal decomposition of ferrous chloride and Se powder in oleylamine [49]. Stoichiometric films of iron selenide with uniform grains were deposited at higher bath temperatures [50]. Nanoflakes of $FeSe_x$ with tetragonal PbO-type were obtained by simple solution-based route in the co-solvent of oleylamine and oleic acid [51].

Nanorods and polyhedra nanorods of Fe_7Se_8 were synthesized by a solvothermal reaction in a mixed solvent of diethylentriamine (DETA) and deionized water (DIW) by changing the solvent ratio [52]. The size tuneable magnetic iron selenide (Fe_3Se_4) nanostructures were prepared by a one-pot high-temperature organic-solution-phase method. The shapes of these nanostructures can be varied from nanosheets and nanocacti, to nanoplates [53, 54]. O'Brien *et al* [55] used *tris*(*N,N*-diethyl-N'-naphthoylselenoureato)iron(III) complex as a single source precursor in oleylamine and produced $FeSe_2$ nanocrystals at temperatures between 190 to 290°C. Sheets and cluster of long rod-shaped crystallites were formed at temperature of 240°C and large cuboid crystallites were prepared at higher 290°C. Uniform thin films of spherical crystallites of FeSe were also deposited from this complex onto silicon substrates by Aerosol Assisted Chemical Vapour Deposition (AACVD) method. The average thickness of the films was 156 nm.

Ubale *et al* [56] reported the deposition of iron selenide thin films onto glass substrate by using chemical bath deposition (CBD) method. The as deposited iron selenide (FeSe) thin films were polycrystalline in nature and showed the optical band gap energy between 2.60 and 2.67 eV, depending on iron ion

concentration in the deposition bath. Colloidal quantum dots of iron selenide capped with biocompatible oleic acid were synthesized by Kamisetti *et al* [57]. Iron selenide quantum dots exhibited intense green fluorescence on exposure to ultraviolet light which was confirmed by photoluminescence spectroscopic study. Rod and plate-like crystallites of iron selenide were synthesised by the thermolysis of *bis*(tetraisopropyldiselenoimidodiphosphinato)-iron(II)and *bis*(tetraphenyldiselenoimidodiphosphinato)iron(II) in oleylamine and hexadecylamine at different growth temperatures [58].

Chen *et al* [59] synthesised the sulphur doped iron selenide nanocrystals to enhance the super conductivity of the material. High quality single-crystals of $FeSe_{1-x}S_x$ system (x = 0, 0.04, 0.09, and 0.11) were prepared. They studied their transport, magnetic and low temperature specific heat properties. The study shows that the introduction of S to FeSe enhances the upper critical field Hc_2, critical current density J*c*, and the T*c*. These properties and its anisotropy are temperature dependent, showing a multiband superconductivity in this system.

Here, we report the simple, inexpensive, and scalable synthesis of iron sulfide, iron selenide and iron sulfo selenide nanoplates by a thermal reaction of iron–oleylamine complexes with sulphur, selenium and mixture of sulphur and selenium powder in oleylamine.

2. Experimental

2.1 Chemicals.

$FeCl_3$ and $FeCl_2$ (anhydrous, 99.99%, Sigma-Aldrich), sulfur and selenium powder (99.998%, Sigma-Aldrich), oleylamine (OA) (80–90%, Acros), Methanol (99.5%, Merck), toluene (99%, Merck) and red S3B dye was taken from native dye industry for photocatalytic degradation. All chemicals were used as received.

2.2 Synthesis of iron sulfide nanoplates

For the synthesis of iron sulphide from iron(III) and iron(II) salt the general method for the preparation of metal sulfide were followed [60]. In a typical reaction 15 ml of olyelamine with 0.81g (5.0 mmol) of $FeCl_3$ in a three-neck flask were heated at 100°C under vacuum for one hour and then under nitrogen for 20 minutes. A solution of S powder (0.96 g (30.0 mmol) dissolved in 10 ml of oleylamine were injected and the temperature was increased and maintained at 230°C for one hour. The mixture was allowed to cool and at 60°C added a mixture of methanol and toluene (1:1) to give a black precipitate of nanoparticles which was separated by centrifugation. The precipitate was washed twice with the mixed solvent (methanol and toluene (1:1)) system. The experiments were also carried out for 30 minutes instead of one hour and using $FeCl_2$ instead of $FeCl_3$.

2.3 Synthesis of iron selenide nanoplates

Iron selenide was prepared by the same method as described under iron sulphide except selenium power was used instead of sulphur.

2.4 Synthesis of iron sulfoselenide nanoplates

Iron sulfoselenide was prepared by the same method using a mixture of sulfur and selenium powder (1:1) in oleylamine.

2.5 Photocatalytic procedure

Photocatalytic activity of as-prepared iron based (FeS_2, $FeSe_2$ and FeSSe) nanoplates were studied for the degradation of reactive red S3B dye (RS3B) under solar light. In typical experiment, 0.02g/L of catalyst was dispersed in 20ppm reactive red S3B solution under sonication followed by magnetically stirring for 30 min in the dark condition to establish the adsorption–desorption equilibrium among the nanoplates and aqueous solution of dye. The sample was then placed under solar light. After every 15 min, 3 to 4 ml aliquot was taken out from the reaction mixture and was centrifuged for 5 min at 8000 rpm to separate the catalyst. The progress of the reaction was checked by calculating the absorbance (A) of the purified filtrate solution at 542 nm (λ_{max}) using UV-Vis spectrophotometer (Shimadzu, UV-1700).

The photocatalytic degradation efficiency (%) was estimated by using the following formula:

$$\text{Degradation \%} = \left(\frac{C_o - C_t}{C_o}\right) \times 100 \quad \text{..... (1)}$$

Where C_o is the initial concentration of dye and C_t is the concentration of dye after photo irradiation at different time intervals. For recyclability, the catalyst was removed after complete degradation reaction by centrifugation then washed with water, ethanol and oven dried.

3. Result And Discussion

Iron sufide, iron selenide and iron sulfo selenide nanoplates were synthesised by using Fe(III) and Fe(II) chloride as iron source and sulfur and selenium powder as S and Se source in oleylamine. The nanoplates were characterized by p-XRD. TEM, HRTEM, SAED EDX and elemental mapping.

3.1 Powder X-ray diffraction of iron sulfide nanoplates

p-XRD patterns of iron sulfide nanoplates obtained from all four experiments i.e. using $FeCl_3$ or $FeCl_2$ in oleylamine for 30 minutes or one hour at 230°C show the pure pyrite (FeS_2) (ICDD NO: 00-042-1340) phase (Fig. 1(a)-(d)). There was no indication for any other phase of iron sulfide. The intensity and the sharpness of the peaks for pyrite phase produced from $FeCl_3$ is lower as compared to those of the pyrite nanoplates obtained from $FeCl_2$ under the same reaction condition. This indicates the better crystallinity

of the material produced from $FeCl_2$ than $FeCl_3$. The clear diffraction peaks for (111), (200), (210), (211), (220), (311), (222), (023) and (321) planes of pyrite (FeS_2) indicates the purity of the material.

3.2 Transmission electron microscopy of iron sulfide nanoplates

TEM images of FeS_2 obtained from all experiments are shown in Fig. 2. Nanoplates produced from $FeCl_3$ and sulfur powder in oleylamine at 230°C after 30 minutes (Fig. 2(a)) reaction are not monodispersed but still we can differentiate plate like morphology of the individual crystallites. HRTEM images (Fig. 2 (b)) shows d-spacing of 2.70 Å correspond to the reflection of (200) plane of pyrite phase. The inset SAED pattern (Fig. 2(b)) shows the polycrystalline nature of the nanoplates. Pyrite nanoplates produced after one hour reaction time from $FeCl_3$ were monodispersed (Fig. 2 (c, d)) having the uniform morphology. HRTEM images (Fig. 2 (e, f)) show the lattice fringes with d-spacing of 2.70 Å and 3.12 Å the reflection of (200 and (111) plane of pyrite.

The nanoploates obtained from Fe (II) chloride and sulfur powder at same reaction conditions shown in Fig. 3 (a, b). These nanoplates are mono-dispersed having well defined shape. The SAED pattern (Fig. 3 (c)) of the crystallites reveals the polycrystalline nature whereas HRTEM analysis (Fig. 3 (d)) shows the d-spacing 3.12 Å correspond to (111) reflection plane of pyrite.

3.3 Iron selenide nanoplates

Figure 4(a,c) shows the p-XRD pattern of the nanoplates obtained from both $FeCl_3$ and $FeCl_2$ with selenium powder in oleylamine at 230°C after 30 minutes whereas (b,d) show the p-XRD patterns of the nanoplates produced after one hour reaction time. All four p-XRD pattern of the iron selenide nanoplates correspond to the mixture of orthorhombic ferrosilite ($FeSe_2$) (ICDD NO: 00-021-0432) and orthorhombic iron selenide ($FeSe_2$) (ICDD NO: 00-011-0565). The diffraction peaks f or ferroselite ($FeSe_2$) (ICDD NO: 00-021-0432) phase were dominant. Only two lower intensity peaks (Fig. 4 (*)) for iron selenide ($FeSe_2$) (ICDD NO: 00-011-0565) phase were observed. It was also observed the intensity of these peaks for this phase decreases with the rise of reaction temperature.

3.4 Transmission electron microscopy of iron selenide nanoplates

TEM images of ferroselite ($FeSe_2$) nanoplates (Fig. 5) obtained from $FeCl_3$ and Se powder after 30 minutes show large clusters of plates as shown in Fig. 5 (a) and HRTEM image of one such plate is shown in Fig. 5 (b). The HRTEM image show clear lattice fringes with d-spacing of 3.69 Å corresponding to (110) reflection plane of ferroselite ($FeSe_2$ (ICDD NO: 00-021-0432) phase. The side view of this image also shows that these plates are comprised of several layers of sheets. Wu *et al.*[61] also reported the iron selenide nanoplates. They explain the mechanism of the formation of nanoplates where covalent bonded Fe and Se slabs were stacked vertically by van der Waals forces. SAED pattern (Fig. 5 (b) inset) reflects the single crystal nature of the product.

The nanoplates of $FeSe_2$ obtained from $FeCl_3$ and selenium powder after one hour reaction time show clusters of plate like crystallites (Fig. 5 (c). HRTEM image (Fig. 5 (d)) shows lattice fringes with d-spacing 5.92 Å corresponding to (101) reflection plane of ferroselite ($FeSe_2$ (ICDD NO: 00-021-0432). The inset in Fig. 5(d) show SAED pattern which indicate the single crystalline nature of $FeSe_2$ nanoplates.

Similar to the iron sulfide nanoplates from $FeCl_2$, the nanoplates of $FeSe_2$ from the $FeCl_2$ and Se powder in oleylamine give different morphology. Plates of different sizes form cluster of crystallites (Fig. 6 (a) for samples obtained from reaction of $FeCl_2$ and Se clearly shows the single crystal nature of the material obtained in oleylamine after 30 minutes (SAED pattern (Fig. 6(b)).

3.5 Iron sulfo selenide nanoplates

The p-XRD patterns obtained from the reaction of $FeCl_2$ or $FeCl_3$ for 30 minutes or 1 hr using a mixture of sulphur and selenium (1:1) are shown in Fig. 7. The experiments carried out for 30 minutes at 230°C give a clear pattern for both $FeCl_2$ or $FeCl_3$ whereas the samples produced after one hour of reaction show comparatively very weak peaks. The strong patterns obtained after 30 minutes from both $FeCl_2$ and $FeCl_3$ are similar but these patterns do not match with either iron sulfide or iron selenide as shown in Figure (7) and the peaks are slightly shifted from both standard patterns of iron sulfide (FeS_2) (ICDD NO: 00-042-1340)) and iron selenide ($FeSe_2$ (ICDD NO: 00-021-0432)) but closer to iron selenide than iron sulfide. This observation is as expected from a pattern of FeS_xSe_{1-x}. There is no standard pattern in the literature for FeS_xSe_{1-x} to compare with.

3.6 Transmission electron microscopy of iron sulfoselenide nanoplates

TEM analysis (Fig. 8 (a)) of iron sulfoselenide obtained from $FeCl_3$ show the formation of irregularly shaped crystallites. A clear difference in the shape and size of the crystallites of iron sulfide, iron selenide and iron sulfoselenide can be seen from the TEM images (Figs. 2, 5 and 8). The entirely different shape of iron sulfoselenide crystals also prove the formation of different material than iron sulphide or iron selenide. The EDX measurements show slightly different atomic percentage of elements (Fe, S, Se) present in the sample (Fig. 8 (b)). The average atomic percentages shown by EDX are Fe: 43.6, S: 10.0, Se: 46.3. This shows the presence of all elements in the ternary material FeSSe. Although sulfur and selenium powders were added in equimolar quantities in the reaction mixture but selenium is found more than four times in the material as compared to sulfur which indicates the higher affinity of iron to selenium as compared to sulfur. This analysis (higher selenium content) corresponds to the p-XRD pattern showing peaks close to the standard pattern of iron selenide as compared to iron sulphide.

TEM images of the samples obtained by the reaction of $FeCl_2$, sulfur and selenium powder in oleylamine at 230°C for 30 minutes (Fig. 9 (a)) show small random crystallites. Electron images (Fig. 9 (b-d)) confirm the presence of all three elements and uniform distribution of iron, sulfur and selenium in the crystallites.

EDX analysis (Fig. 9 (e)) shows the Fe, S and Se ratio as Fe: 42.98, S: 12.32, Se: 44.70 which is close to that found for similar reaction of $FeCl_3$.

3.7 Photocatalytic activity

The photocatalytic behavior of synthesized iron based nanoplates (FeS, FeSe and FeSSe) were calculated by measuring the degradation rate of azoic red S3B (RS3B) dye solution under solar light at room temperature. The uv/vis absorption spectrum for RS3B aqueous solution with the initial concentration of 20 mg/L was described in Fig. 10(a). The maximum absorption peak of RS3B was observed at 543 nm before and after illumination.

The relationship between the absorbance and irradiation time of reactive dye RS3B in the presence of synthesized iron based catalysts (FeS, FeSe and FeSSe nanoplates) under solar light for 105 min which shows that the absorbance decreased with the increase of reaction time due to the decrease in concentration of dye (RS3B) and also decomposition of organic compound in the solution as shown in Fig. 10 (b). RS3B aqueous solution (25 mL) with initial concentration of dye was 20 mg/L and fixed amount of photocatalyst (0.02 g/L) was loaded and exposed to solar light at a time interval of 15 min for 105 min to ensure the photodegradation effect. The mild red color of the initial solution of the RS3B gradually decolorized during the photocatalytic reaction with the passing of irradiation time as shown in Fig. 11(a) and (b). After catalyst loading, the degradation efficiency increased upto 0.02g/L and then it goes to decreases progressively. It may be due to the scattering and low light penetration in the dye solution as increased the concentration catalyst, the active molecules start colliding at lower energy level and become deactivated so rate of reaction will be low. Figure 12 (a-c) represents the comparison of photodegradation efficiency of FeS, FeSe and FeSSe nanoplates which are synthesized by using different precursors and various time at constant temperature 230 ^{o}C under solar light irradiation The degradation efficiency of RS3B is calculated and investigated with or without synthesized nanoplates as a photocatalyst with Eq. (1). RS3B solution shows negligible degradation without catalyst after 105 min. But dye degradation efficiency was increased with photocatalyst. Catalytic activity of synthesized nanoplates is increased with the increase of surface area of the nanoplates, so that the nanoplates obtained from Fe (II) chloride and sulfur powder in OLA at 230 ^{o}C after 30 min reaction time has the larger specific surface area as compared to obtained from Fe (III) chloride at the same reaction conditions as depicted in Fig. 12 (a-c). The rate of photodegradation is increased with larger surface to volume ratio which permits more dye molecules to be adsorbed onto the surface of the photocatalyst [62].

The degradation efficiency of RS3B in the presence of different forms of FeS_2 nanoplates (A-D) is 35.1%, 40.2%, 60% and 79% respectively as depicted in Fig. 12 (a). To investigate the effect of reaction time and iron source on the photoactivity of FeS_2 nanoplates, the catalytic behavior of the nanoplates was performed. It was observed that Fe (II) is better source of iron and synthesis carried out 30 minutes give much better quality material than those for one hour. This observation was true for all three photocatalysts (FeS_2, $FeSe_2$ and FeSSe) as depicted in Fig. 12 (a-c). Also for $FeSe_2$ nanoplates, the degradation of RS3B was investigated and observed that nanoplates of $FeSe_2$ obtained from Fe (II)

source at 30 min shows better degradation efficiency (80.3%) as compared to Fe (III) source nanoplates percentage of dye degradation (39%). From Fe (II) source the degradation efficiency of $FeSe_2$ increased from 62.4 to 80.2% as compared $FeSe_2$ nanoplates (29.9 to 35.8%) obtained from Fe (III) source at mentioned reaction times as shown in Fig. 12 (b).

The ternary material (FeSSe) shows the better degradation efficiency as compared to FeS_2 and $FeSe_2$ nanoplates. It is seen in Fig. 12 (d), higher dye degradation activity of FeSSe (85.3%) as compared to the FeS_2 (79%) and $FeSe_2$ (80.2%) nanoplates obtained from Fe (II) source and 30 min reaction time at constant temperature.

The dye concentration left after responding with the photocatalyst as shown in Fig. 13 (a). Firstly, pure dye was bared in the absence of catalyst to the solar light which indicates that absorption of the dye solution was remained same, it is concluded that no environmental changes on the dye solution. As we exposed the solution of RS3B to solar light in the presence of FeS_2, $FeSe_2$ and FeSSe nanoplates then a substantial removal and degradation was observed. The rate of degradation was almost same (79.7% and 80.1%) with FeS_2 and $FeSe_2$ respectively as shown in the Fig. 13 (a), but the ternary materials of FeSSe nanoplats showed the most percentage degradation (85.3%) of RS3B dye as labeled (E) in Fig. 13 (a).

Photo-stability and reusability of the photocatalyst was checked through repeating the RS3B degradation experiments reusing the same nanoplates. The nanoplates were used five run of photo catalytic process for 105 min of each run and nanoplates cleaned for subsequent use. Photocatalytic activity of the nanoplates of FeS_2, $FeSe_2$ and FeSSe shows the same behavior as RS3B removal after five recycling run are represented in Fig. 13 (b), the photocatalytic performance of nanoplates does not display any flagrant reduction for RS3B dye removal which confirms that the nanoplates is a photostable catalyst and are not corroded easily during the reaction process.

The kinetics of dye degradation was roughly measured for RS3B based on the data plotted in Fig. 12 (a-c). To check the kinetic rate of RS3B photodegradation process onto FeS_2, $FeSe_2$ and FeSSe nanoplates, pseudo first order kinetic model was applied on the experimental data and commonly used the formula as

$$\ln\left(\frac{C_t}{C_o}\right) = kt \qquad \text{.....(2)}$$

Where k is the rate constant (min^{-1}) and Ct and Co are the concentrations (mg/L) of dye at various time intervals and initially used respectively. The straight line graph obtained which shows that the reaction obey the first order kinetic model [63] as results are shown in Fig. 14. The average value of R^2 (correlation coefficient) for FeS_2, $FeSe_2$ and FeSSe was 0.96, which confirm that dye photo degradation process

satisfies the first order kinetic model. The rate constants of dye were 0.18, 0.21 and 0.08 min^{-1}, for FeS_2, $FeSe_2$ and FeSSe respectively.

4. Conclusions

Iron sulfide, iron selenide and iron sulfur selenide have been synthesized by a facile method by using Fe (III) and Fe (II) chloride as iron source and sulfur and selenium powder as S and Se source in oleylamine. The comparison of crystallinity, dimensions, yields and electronic properties of these two-dimensional nanoplates with respect to the use of Fe (II) or Fe (III) as iron source and also the synthesis carried out at 30 minutes and one hour show that Fe (II) is better source for iron and the synthesis carried out at 30 minutes give much better quality materials that those synthesized for one hour. This observation was true for all three materials (FeS_2, $FeSe_2$ and FeSSe). The p-XRD for the ternary material clearly showed the composite nature of this material (by shifting the XRD peaks in between FeS_2 and $FeSe_2$) rather than a mixture of FeS_2 and $FeSe_2$. The composite nature of the ternary material is also showed by the elemental mapping images which show the uniform distribution of iron, sulfur and selenium. These iron based non-toxic nanoplates are stable for long periods and showed a good photocatalytic activity against carcinogenic dye RS3B. The effluents of other toxic dyes can be degraded by using these non-toxic, low cost nanoplates. This simple synthetic method is very useful to produce high quality of either binary or ternary phases of iron based nanoplates for photocatalysis applications. The sulfur or selenium content can easily be controlled to tune the band gap of this material and improve their photocatalysis efficiency.

References

1. Hou, Y., Z. Xu, and S. Sun, *Controlled synthesis and chemical conversions of FeO nanoparticles.* Angewandte Chemie International Edition, 2007. **46**(33): p. 6329-6332.
2. Zeng, H. and S. Sun, *Syntheses, properties, and potential applications of multicomponent magnetic nanoparticles.* Advanced Functional Materials, 2008. **18**(3): p. 391-400.
3. Kamat, P.V., *Quantum dot solar cells. Semiconductor nanocrystals as light harvesters.* The Journal of Physical Chemistry C, 2008. **112**(48): p. 18737-18753.
4. Rajeshwar, K., N.R. de Tacconi, and C. Chenthamarakshan, *Semiconductor-based composite materials: preparation, properties, and performance.* Chemistry of Materials, 2001. **13**(9): p. 2765-2782.
5. Wadia, C., A.P. Alivisatos, and D.M. Kammen, *Materials availability expands the opportunity for large-scale photovoltaics deployment.* Environmental science & technology, 2009. **43**(6): p. 2072-2077.
6. Ahuja, R., A. Sidhu, and A. Bala, *Synthesis and evaluation of iron (ii) sulfide aqua nanoparticles (FeS-NPs) against Fusarium verticillioides causing sheath rot and seed discoloration of rice.* European Journal of Plant Pathology, 2019: p. 1-9.
7. Horwitz, N.E., et al., *Redox-Active 1D Coordination Polymers of Iron-Sulfur Clusters.* Journal of the American Chemical Society, 2019.

8. Liu, M., *Solution-phase synthesis and characterization of fe2ges4 material and photovoltaic devices.* 2019.
9. Le Donne, A., V. Trifiletti, and S. Binetti, *New Earth-Abundant Thin Film Solar Cells Based on Chalcogenides.* Frontiers in Chemistry, 2019. **7**.
10. Ojo, A., W. Cranton, and I. Dharmadasa, *Introduction to Photovoltaics*, in *Next Generation Multilayer Graded Bandgap Solar Cells*. 2019, Springer. p. 1-15.
11. Prabaharan, N., M.A. Rosen, and P.E. Campana, *Recent Developments in Photovoltaic Materials and Devices*. 2019.
12. Matthews, P.D., et al., *Synthetic routes to iron chalcogenide nanoparticles and thin films.* Dalton Transactions, 2016. **45**(47): p. 18803-18812.
13. Zhang, M., et al., *A novel synthesis of Fe7S8@ Fe5Ni4S8 flower center/petal hierarchical nanostructure: Application as advance cathode material for high-performance supercapacitors.* Journal of colloid and interface science, 2019. **536**: p. 609-617.
14. Wu, L., *Transition metal chalcogenide based functional materials for renewable energy conversion.* 2019.
15. Jasion, D., et al., *Low-dimensional hyperthin FeS2 nanostructures for efficient and stable hydrogen evolution electrocatalysis.* ACS Catalysis, 2015. **5**(11): p. 6653-6657.
16. Wang, Y.-X., et al., *Uniform yolk-shell iron sulfide–carbon nanospheres for superior sodium–iron sulfide batteries.* Nature communications, 2015. **6**: p. 8689.
17. Barawi, M., et al., *Hydrogen photoassisted generation by visible light and an earth abundant photocatalyst: pyrite (FeS2).* The Journal of Physical Chemistry C, 2016. **120**(18): p. 9547-9552.
18. Khalid, S., et al., *Nanocrystalline Pyrite for Photovoltaic Applications.* Chemistryselect, 2018. **3**(23): p. 6488-6524.
19. Xu, X., et al., *Pomegranate-like mesoporous microspheres assembled by N-doped carbon coated Fe1− xS nanocrystals for high-performance lithium storage.* Journal of Alloys and Compounds, 2019.
20. Puthussery, J., et al., *Colloidal iron pyrite (FeS2) nanocrystal inks for thin-film photovoltaics.* Journal of the American Chemical Society, 2010. **133**(4): p. 716-719.
21. Chen, X., et al., *Single-source approach to cubic FeS2 crystallites and their optical and electrochemical properties.* Inorganic chemistry, 2005. **44**(4): p. 951-954.
22. Findlay, A.J., et al., *Iron and sulfide nanoparticle formation and transport in nascent hydrothermal vent plumes.* Nature communications, 2019. **10**(1): p. 1597.
23. Wang, D., Q. Wang, and T. Wang, *Shape controlled growth of pyrite FeS 2 crystallites via a polymer-assisted hydrothermal route.* CrystEngComm, 2010. **12**(11): p. 3797-3805.
24. Kar, S. and S. Chaudhuri, *Solvothermal synthesis of nanocrystalline FeS2 with different morphologies.* Chemical physics letters, 2004. **398**(1-3): p. 22-26.
25. Gadisa, B.T., R. Appiah-Ntiamoah, and H. Kim, *Amorphous iron sulfide nanowires as an efficient adsorbent for toxic dye effluents remediation.* Environmental Science and Pollution Research, 2019.

26(3): p. 2734-2746.

26. Li, W., et al., *Pyrite nanocrystals: shape-controlled synthesis and tunable optical properties via reversible self-assembly.* Journal of Materials Chemistry, 2011. **21**(44): p. 17946-17952.
27. Roberts, D.M., S.E. Russek, and C.R. Stoldt, *Synthetic iron pyrite across length scales: interfacial defects and macroscopic properties.* CrystEngComm, 2019.
28. Kirkeminde, A., et al., *Synthesis and optoelectronic properties of two-dimensional FeS2 nanoplates.* ACS applied materials & interfaces, 2012. **4**(3): p. 1174-1177.
29. Steinhagen, C., et al., *Pyrite nanocrystal solar cells: promising, or fool's gold?* The journal of physical chemistry letters, 2012. **3**(17): p. 2352-2356.
30. Macpherson, H.A. and C.R. Stoldt, *Iron pyrite nanocubes: size and shape considerations for photovoltaic application.* Acs Nano, 2012. **6**(10): p. 8940-8949.
31. Morrish, R., R. Silverstein, and C.A. Wolden, *Synthesis of stoichiometric FeS2 through plasma-assisted sulfurization of Fe2O3 nanorods.* Journal of the American Chemical Society, 2012. **134**(43): p. 17854-17857.
32. Marquardt, J., *Structure property relations in chalcopyrite based intermediate band solar absorber materials*. 2019.
33. Cummins, D.R., et al., *Iron sulfide (FeS) nanotubes using sulfurization of hematite nanowires.* Nano letters, 2013. **13**(6): p. 2423-2430.
34. Beal, J.H., P.G. Etchegoin, and R.D. Tilley, *Synthesis and characterisation of magnetic iron sulfide nanocrystals.* Journal of Solid State Chemistry, 2012. **189**: p. 57-62.
35. Wang, X., et al., *Solvent-free Synthesis of Hexagonal Iron Sulfide Nanoflowers.* Chinese Journal of Chemistry, 2013. **31**(8): p. 983-986.
36. Di Giovanni, C., et al., *Bioinspired iron sulfide nanoparticles for cheap and long-lived electrocatalytic molecular hydrogen evolution in neutral water.* Acs Catalysis, 2014. **4**(2): p. 681-687.
37. Vanitha, P. and P. O'Brien, *Phase Control in the Synthesis of Magnetic Iron Sulfide Nanocrystals From a Cubane-Type Fe− S Cluster.* Journal of the American Chemical Society, 2008. **130**(51): p. 17256-17257.
38. Wadia, C., et al., *Surfactant-assisted hydrothermal synthesis of single phase pyrite FeS2 nanocrystals.* Chemistry of materials, 2009. **21**(13): p. 2568-2570.
39. Beal, J.H., P.G. Etchegoin, and R.D. Tilley, *Transition metal polysulfide complexes as single-source precursors for metal sulfide nanocrystals.* The Journal of Physical Chemistry C, 2010. **114**(9): p. 3817-3821.
40. Abdelhady, A.L., et al., *Nickel and iron sulfide nanoparticles from thiobiurets.* The Journal of Physical Chemistry C, 2012. **116**(3): p. 2253-2259.
41. Akhtar, M., et al., *The synthesis of iron sulfide nanocrystals from tris (O-alkylxanthato) iron (III) complexes.* Journal of Materials Chemistry A, 2013. **1**(31): p. 8766-8774.

42. Akhtar, M., et al., *Deposition of iron sulfide nanocrystals from single source precursors.* Journal of Materials Chemistry, 2011. **21**(26): p. 9737-9745.
43. Han, W. and M. Gao, *Investigations on iron sulfide nanosheets prepared via a single-source precursor approach.* Crystal Growth and Design, 2008. **8**(3): p. 1023-1030.
44. Bi, Y., et al., *Air stable, photosensitive, phase pure iron pyrite nanocrystal thin films for photovoltaic application.* Nano letters, 2011. **11**(11): p. 4953-4957.
45. Akhtar, M., et al., *Deposition of iron sulfide thin films by AACVD from single source precursors.* Journal of Crystal Growth, 2012. **346**(1): p. 106-112.
46. Li, W., et al., *Optical and electronic properties of pyrite nanocrystal thin films: the role of ligands.* Small, 2014. **10**(6): p. 1194-1201.
47. Wu, X., et al., *Two-carrier transport and ferromagnetism in FeSe thin films.* Journal of Applied Physics, 2008. **103**(11): p. 113501.
48. Hsu, F.-C., et al., *Superconductivity in the PbO-type structure α-FeSe.* Proceedings of the National Academy of Sciences, 2008. **105**(38): p. 14262-14264.
49. Lin, C.-R., et al., *Magnetic properties of iron selenide nanocrystals synthesized by the thermal decomposition.* IEEE Transactions on Magnetics, 2009. **45**(10): p. 4275-4278.
50. Thanikaikarasan, S., et al., *Growth and characterization of electrosynthesized iron selenide thin films.* Vacuum, 2009. **83**(7): p. 1066-1072.
51. Chen, L., et al., *Composition and size tailored synthesis of iron selenide nanoflakes.* CrystEngComm, 2010. **12**(12): p. 4386-4391.
52. Gao, M.R., et al., *Selective Synthesis of Fe7Se8 Polyhedra with Exposed High-Index Facets and Fe7Se8 Nanorods by a Solvothermal Process in a Binary Solution and Their Collective Intrinsic Properties.* Chemistry–A European Journal, 2011. **17**(18): p. 5068-5075.
53. Zhang, H., et al., *Fe3Se4 nanostructures with giant coercivity synthesized by solution chemistry.* Chemistry of Materials, 2011. **23**(16): p. 3769-3774.
54. Ulbrich, K. and C. Campos, *Stability of iron selenide nanophases prepared by mechanosynthesis.* AIP Advances, 2019. **9**(4): p. 045311.
55. Akhtar, M., et al., *Deposition of iron selenide nanocrystals and thin films from tris (N, N-diethyl-N'-naphthoylselenoureato) iron (iii).* Journal of Materials Chemistry, 2012. **22**(30): p. 14970-14975.
56. Ubale, A.U. and S.G. Ibrahim, *Structural, electrical and optical properties of nanocrystalline Cd1−xFexSe thin films deposited by chemical spray technique.* Journal of Saudi Chemical Society, 2015. **19**(6): p. 667-675.
57. Mulpur, P., T.M. Rattan, and V. Kamisetti, *One-step synthesis of colloidal quantum dots of iron selenide exhibiting narrow range fluorescence in the green region.* Journal of Nanoscience, 2013. **2013**.
58. Akhtar, M., et al., *Synthesis of iron selenide nanocrystals and thin films from bis (tetraisopropyldiselenoimidodiphosphinato) iron (II) and bis*

(tetraphenyldiselenoimidodiphosphinato) iron (II) complexes. Journal of Materials Chemistry A, 2014. **2**(48): p. 20612-20620.

59. Abdel-Hafiez, M., et al., *Superconducting properties of sulfur-doped iron selenide.* Physical Review B, 2015. **91**(16): p. 165109.
60. Joo, J., et al., *Generalized and facile synthesis of semiconducting metal sulfide nanocrystals.* Journal of the American Chemical Society, 2003. **125**(36): p. 11100-11105.
61. Chen, L., et al., *Facile Solvothermal Synthesis of Uniform Iron Selenide Nanoplates.* European Journal of Inorganic Chemistry, 2011. **2011**(13): p. 2098-2102.
62. Lv, J., et al., *Effect of annealing temperature on photocatalytic activity of ZnO thin films prepared by sol–gel method.* Superlattices and Microstructures, 2011. **50**(2): p. 98-106.
63. Khan, H.R., et al., *Photocatalytic removal of carcinogenic reactive red S3B dye by using ZnO and Cu doped ZnO nanoparticles synthesized by polyol method: A kinetic study.* Solar Energy, 2018. **173**: p. 875-881.

Figures

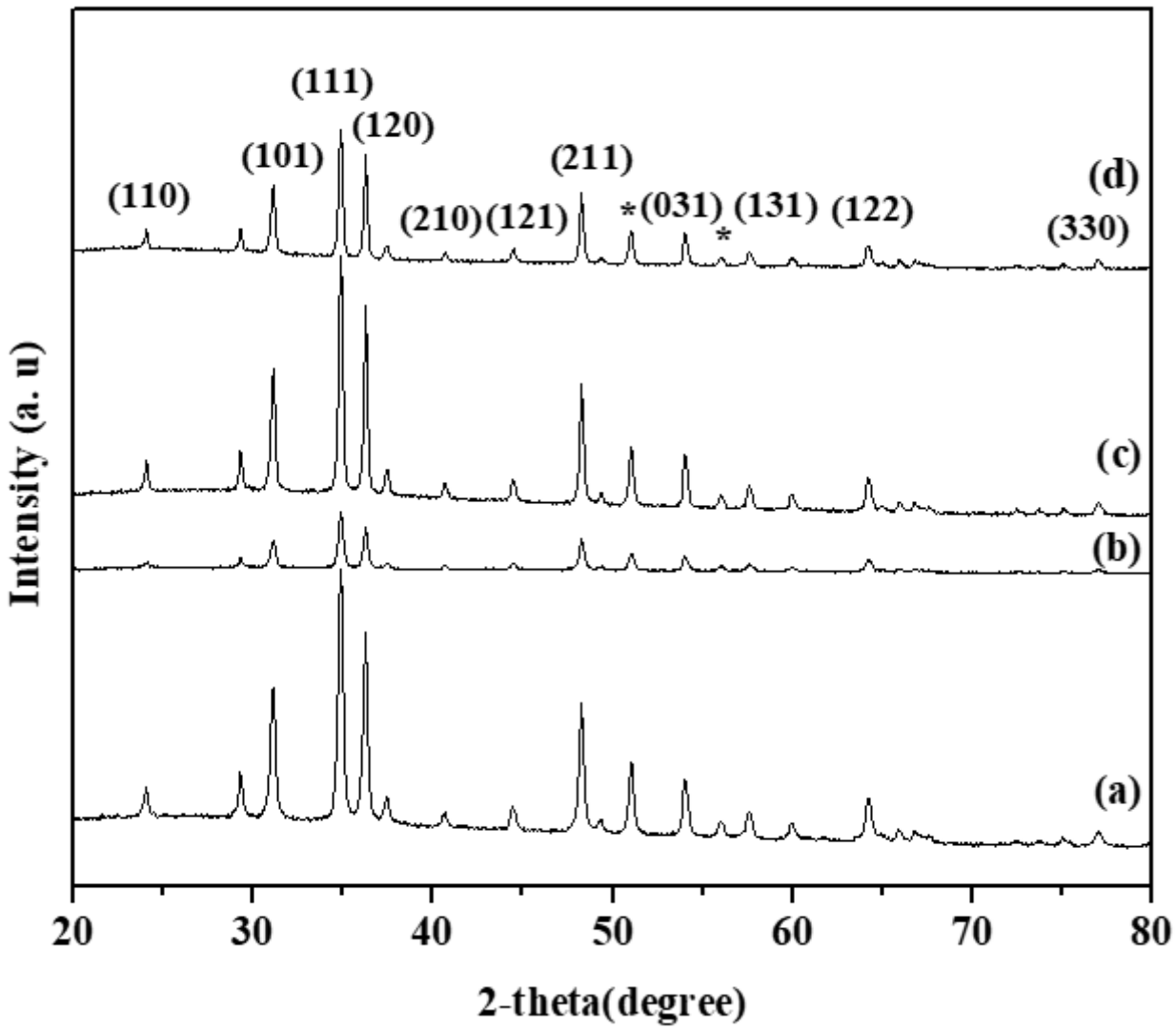

Figure 4

p-XRD pattern for ferroselite ($FeSe_2$) nanoploates obtained from Fe(III) chloride and selenium powder in oleylamine at 230 °C **(a)** 30 minutes **(b)** 1 hour and Fe(II) chloride and selenium powder **(c, d)** after 30 minutes and 1 hour reaction time. The (*) shows another iron selenide ($FeSe_2$) phase.

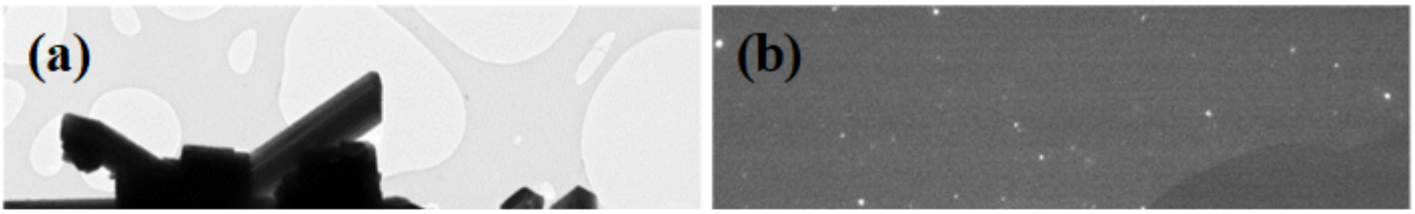

Figure 6

(a) Growth of $FeSe_2$ nanoplates in oleylamine at 230°C from $FeCl_2$ and Se powder after 30 minutes **(b)** SAED pattern of crystallites.

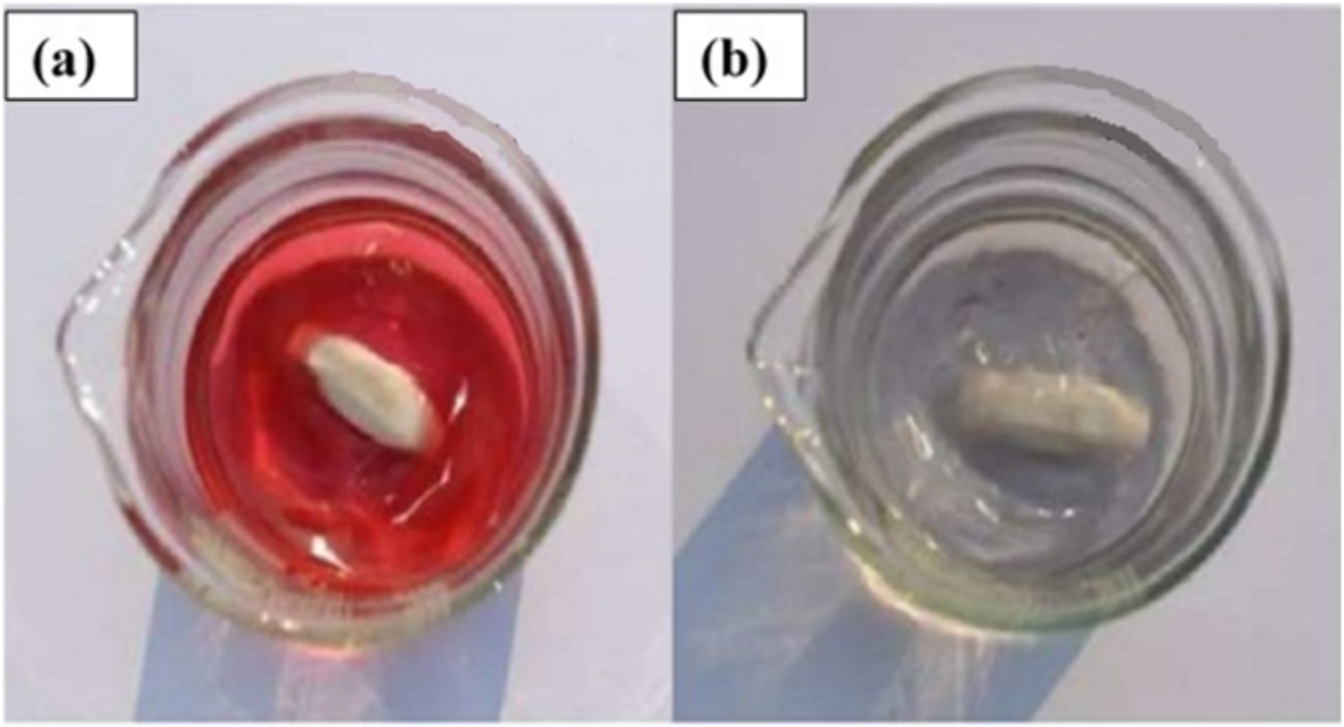

Figure 11

Photocatalytic reaction with the passing of irradiation time (a) before irradiation time (b) after irradiation time

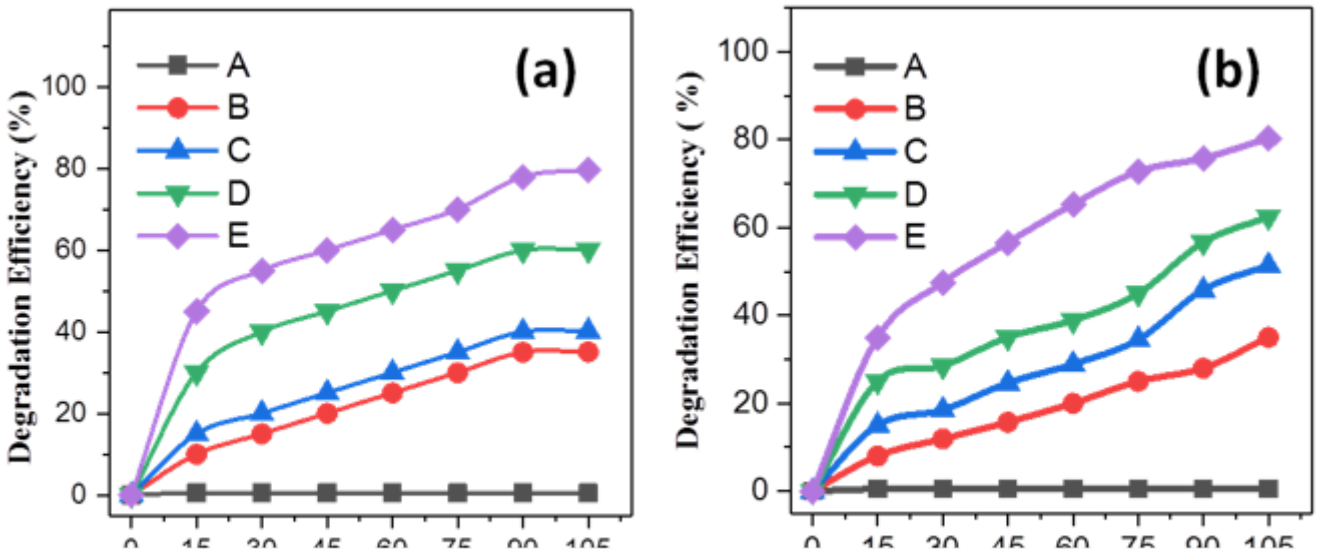

Figure 12

Comparison of photodegradation efficiencies of RS3B in the absence and presence of solar light **(a-c)** for FeS, $FeSe_2$ and FeSSe nanoploates respectively, (A, B) from $FeCl_3$ for one hr and 30 min reaction time respectively, (C,D) $FeCl_2$ after one hour and 30 min reaction time, **(d)** percentage degradation of (A) RS3B dye in the dark (B)RS3B solution in FeS_2 (C) RS3B solution in $FeSe_2$ (D) RS3B solution in FeSSe obtained from Fe (II) chloride and sulfur/Se powder after 30 minutes at 230 ^oC.

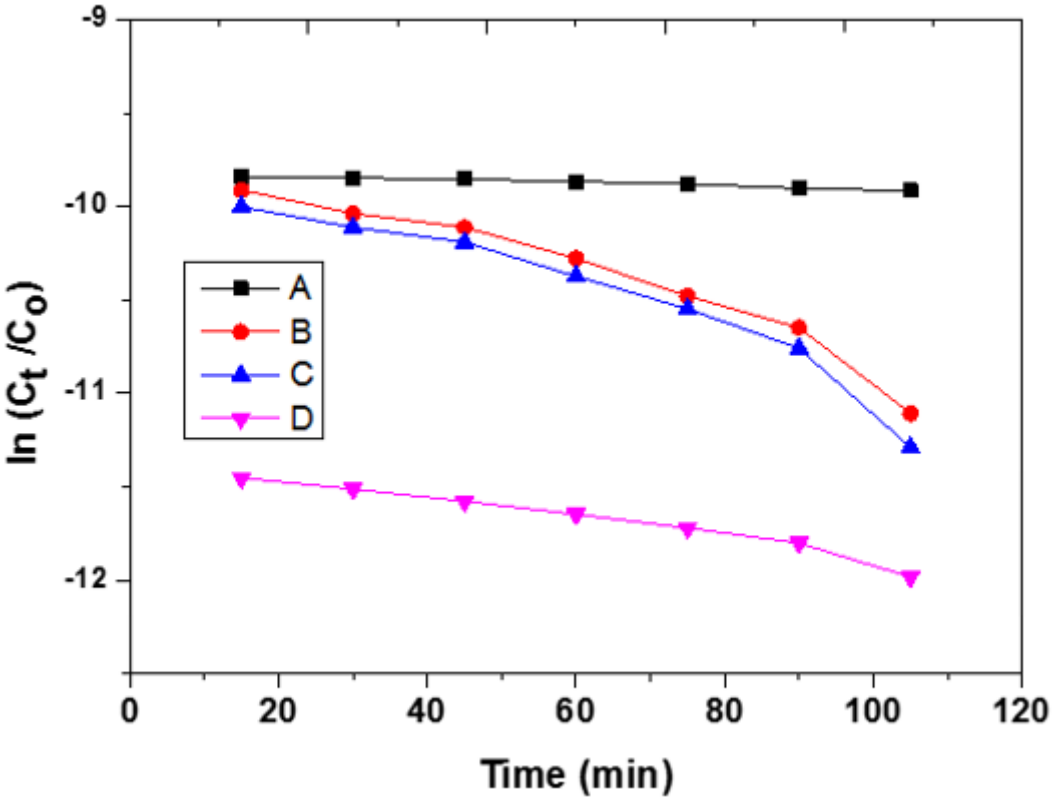

Figure 14

Kinetic curves for photocatalytic degradation of (A) RS3B dye in dark and (B-D) RS3B solution in the existence of FeS_2, $FeSe_2$ and FeSSe obtained from Fe (II) chloride and sulfur/selenium powder after 30 minutes reaction time. (20mg/L initial concentration of solution and catalyst dose 0.02 g/L).

Supplementary Files

This is a list of supplementary files associated with this preprint. Click to download.

- scheme1.png